Lung injury induces alveolar type 2 cell hypertrophy and polyploidy with implications for repair and regeneration

Anthea Weng[1], Mariana Maciel-Herrerias[1], Satoshi Watanabe[1], Lynn Welch[1], Annette S. Flozak[1], Rogan Grant[1], Raul Piseaux Aillon[1], Laura Dada[1], Seung Hye Han[1], Monique Hinchcliff[3], Alexander Misharin[1], GR Scott Budinger[1], Cara J. Gottardi[1,2]*

Northwestern University, Feinberg School of Medicine
[1]Department of Pulmonary Medicine, [2]Biochemistry and Molecular Genetics
Chicago, IL 60611, USA

[3]Department of Medicine, Division of Rheumatology, Allergy and Immunology, Yale University School of Medicine
New Haven, CT 06510 USA

Running title: Injury-induced alveolar epithelial polyploidization

Corresponding author*:
Cara J. Gottardi
303 East Superior Street
Simpson-Querrey 5-525
Chicago, IL 60611, USA
c-gottardi@northwestern.edu
312-503-4123

4378 (Abstract, Results, Discussion, Figure legends; minus Methods) words
7 Figures

Abstract

Epithelial polyploidization post-injury is a conserved phenomenon, recently shown to improve barrier restoration during wound healing. Whether lung injury can induce alveolar epithelial polyploidy is not known. We show that bleomycin injury induces AT2 cell hypertrophy and polyploidy. AT2 polyploidization is also seen in short term ex vivo cultures, where AT2-to-AT1 trans-differentiation is associated with substantial binucleation due to failed cytokinesis. Both hypertrophic and polyploid features of AT2 cells can be attenuated by inhibiting the integrated stress response (ISR) using the small molecule ISRIB. These data suggest that AT2 polyploidization may be a feature of alveolar epithelial injury. As AT2 cells serve as facultative progenitors for the distal lung epithelium, a propensity for injury-induced binucleation has implications for AT2 self-renewal and regenerative potential upon re-injury, which may benefit from targeting the ISR.

Keywords: Alveolar epithelial cell, injury, binucleation, polyploidy, cytokinesis, integrated stress response

Introduction

Although most patients recover from severe lung injury induced by SARS-CoV-2 pneumonia or other insults, some will develop persistent and progressive lung fibrosis (1-3), highlighting a growing imperative to understand how the distal lung epithelium repairs after injury (1, 3-6). While it is clear surfactant producing-alveolar type 2 pneumocytes (AT2 cells) are progenitors that give rise to alveolar type 1 pneumocytes (AT1 cells)(7, 8), the variability between individuals in the AT2-to-AT1 cell trans-differentiation program to restore normal alveolar function is unexplained.

Pathologists have long recognized that a range of injurious stimuli lead to the accumulation of abnormally large AT2 cells, described as “hypertrophic or hyperplastic” AT2 cells (9-12). Morphologically similar cells are seen in autopsy specimens or lung explants from patients with lung injury secondary to SARS-CoV-2 pneumonia (1, 5), but mechanisms underlying this cell state and its consequences for lung repair post-injury remain puzzling. A recent convergence of single cell transcriptomic-studies from a range of mouse injury models suggests that instead of fully progressing to an AT1 cell fate, AT2 cells become stalled at an intermediate transition-state characterized by activation of cell cycle arrest pathways (p16, p21, p53),TGFβ signaling and matrix remodeling (SERPINE1)(13-16). Serially collected single cell RNA-sequencing data over the course of bleomycin induced injury shows the formation of this intermediate transition state is preceded by increased expression of genes in the integrated stress response (ISR)(15). In tissue sections, these transitional cells are characterized by elevated levels of specific intermediate filament keratins (KRT8/18 in mice; KRT17 in humans) and other structural proteins, along with an intermediate AT2-to-AT1 morphology (15, 16). These data suggest small cuboidal AT2 cells differentiate into large and flattened AT1 cells through a morphologically stressful transition that appears prone to stalling after injury. Importantly, recent evidence suggests the AT2-to-AT1 transition state is not fixed, as therapeutic targeting of p53 or ISR signaling appears to guide AT2 cells through this vulnerable trans-differentiation step (16, 17). However, the cellular processes most vulnerable to this morphogenetic transition, which drives persistence of the AT2-to-AT1 transition state in injured lungs, and can be reversed by these the therapies are unknown.

Epithelial polyploidization and consequent hypertrophy post-injury is a conserved phenomenon observed from flies to vertebrates (18). It is a process by which cells increase their DNA content and bypass mitosis. Polyploid cells are larger than their diploid counterparts because cell size

82 scales with DNA content (19). Cell hypertrophy is advantageous during epithelial repair, as
83 larger cells manifest less junctional surface area per unit of epithelium, leading to decreased
84 permeability in an otherwise leaky-barrier environment (20, 21). Increased DNA copies can also
85 favor adaptation to cell and environmental stress, in ways that are context and injury dependent
86 (22-24). However, these benefits of polyploidization come at a cost, as polyploid cells will less
87 faithfully segregate DNA during mitosis (25-27). Thus, polyploidization of differentiated cell
88 types—particularly those that serve also as progenitors (e.g., AT2 cells)—is likely to adversely
89 impact future regenerative potential of the tissue. Whether AT2 polyploidy underlies injury-
90 induced AT2 hypertrophy and drives persistence of the AT2-to-AT1 cell stalled state is
91 unknown.
92
93 In this study, we show that lung injury leads to AT2 hypertrophy and polyploidization—notably
94 binucleated AT2s—during the acute injury response. *Ex vivo* analysis suggests the route to
95 polyploidy is via failed cytokinesis during the AT2-to-AT1 flattening process. A small molecule
96 inhibitor of the integrated stress response, ISRIB, which we have previously shown ameliorates
97 fibrosis development in murine models (17), inhibits the abundance of hypertrophic, polyploid
98 AT2 cells. These data suggest that modulating stress signals during the morphogenetically
99 challenging AT2-to-AT1 transition may improve key steps through which injured AT2 cells divide
100 and differentiate to restore the alveolar epithelium. Implications of failing to remove and replace
101 polyploid AT2 cells after lung injury are discussed.

102 **Results**

103 **Lung injury induces AT2 hypertrophy**

104 To understand how lung injury alters the morphogenetic sequence by which AT2 cells grow,
105 divide and differentiate to an AT1 fate, we used a genetic lineage tracing system to permanently
106 label AT2 cells in *Sftpc*$^{Cre\text{-}ER}$; $^{Lox\text{-}Stop\text{-}Lox}$zsGreen mice subjected to the bleomycin model of injury
107 and fibrogenic repair (17) (Fig.1A). As with previous studies (9-12), we confirm that bleomycin
108 injury leads to zsGreen+ cells that are larger than AT2 lineage-labeled mice exposed to saline
109 (Fig. 1B and C, quantification from 2 mice, 5 fields of view; Frozen section image analysis
110 pipeline in Fig. S1A). Cell size difference may be more readily apparent in 14μm thick frozen
111 sections than thinner 4μm paraffin sections, likely because the former method favors cell
112 visualization along a greater portion of the curved alveolus (Fig. S1B). The injury-induced size
113 increase is not an aberrant feature of cells expressing the fluorescence lineage-label, as AT2
114 cells lacking zsGreen but expressing surfactant protein C (SpC) also increase in size (Fig.
115 S1C). Lastly, we can also detect this size increase by flow cytometric analysis of AT2 cells (Fig.
116 S2A-C; Median Forward Scatter Area quantification from 3 mice/condition), demonstrating the
117 injury-induced phenotype is not an artefact of lung fixation or processing.
118

119 **Lung injury promotes AT2 cell polyploidization**

120 As cell size can scale with DNA context (19), we sought to examine nuclear features of
121 hypertrophic AT2 cells. Interestingly, we found a number of lineage-labeled AT2 cells with two
122 nuclei (Fig. 2A), often observing 1-2 binucleated zsGreen+ cells per field of view, estimating a
123 rate of ~8% (Fig. 2B; see also Fig.1B inset box). To validate AT2 polyploidy via an independent
124 method, we sought to quantify and characterize these cells by flow cytometry paired with DNA
125 content analysis (Fig. S2A-E). Although we readily detected AT2 cells with 2N or 4N DNA
126 content, too few 4N cells survived the cytospin procedure to reliably quantify binucleation rate
127 differences between saline and bleomycin-treated mice (Fig. S2E). New methods will be
128 required to reliably isolate and quantify this apparently fragile cell state.

129 Of interest, AT2 binucleation appears compatible with expression of the AT1 marker, podoplanin
130 (Fig. 2A-a' magenta arrow), but we can also detect binucleated cells expressing the AT2
131 marker, surfactant protein C (SpC) (Fig. S2F). These data suggest alveolar epithelial polyploidy
132 may be compatible with either AT2 or AT1 cell state. To address wither AT2 polyploidy is a
133 typical feature of the recently described AT2-to-AT1 cell transition state (14, 15), we
134 interrogated Krt8 expression in our lung sections. While we can find large binucleated cells that
135 highly express Krt8 protein, AT2 binucleation does not exclusively correlate with a Krt8-high

136 state (Fig. 3). Remarkably, binucleation is a common feature of primary AT2 cultures grown on
137 glass or filters (Fig. 4). We are confident these *ex vivo* polyploid cells derive from *bona fide* AT2
138 cells, as they are uniformly Krt8-positive (Fig. 4A) and can be lineage-labeled using the *Sftpc*-
139 $^{\text{CreER; Lox-stop-Lox eYFP}}$ system (Fig. 4B,C). Even AT2-derived organoids, which can show AT2-to-
140 AT1 cell transition state features seen in injured lungs (16), exhibit a binucleation rate similar to
141 *in vivo* estimates (Fig. 4E,F vs Fig. 2B). Mechanistically, live-imaging reveals binucleated cells
142 can be generated via failed cytokinesis, further suggesting that how AT2 polyploidy is generated
143 and maintained can be interrogated in *ex vivo* cultures (Fig. 5).

144 Given limitations of assessing polyploidy from frozen or thick sectioning (Fig. S1B), together
145 with evidence that mononuclear polyploidy also exists (28), we sought an independent method
146 to assess the polyploidy rate in injured AT2 cells. A recent study showed that the stochastic,
147 multi-color Confetti reporter system can be used to assess mononuclear polyploidy in mouse
148 tissues, notably liver (29). While the Confetti reporter mouse is better known for tracing clonal
149 cell relationships in development and injury (8, 30), this tool can also validate polyploid cells in
150 tissues with single cells expressing two or more fluorescent proteins (Fig. S3A). In contrast to
151 cell clone tracing, the lineage label must be activated by tamoxifen *after genome duplication* to
152 detect single cell polyploidy. By subjecting *Sftpc*$^{\text{Cre-ER}}$ x *Rosa*^{Confetti} mice to the bleomycin model
153 of injury, we could identify large, partially flattened cells that express both green fluorescent
154 protein (GFP) and red fluorescent protein (RFP) lineage labels surrounding what appears as a
155 single nucleus of lineage-label exclusion (Fig. S3B,C). We also identified small round,
156 GFP/RFP-dual-positive cells that likely reflect lineage-labeled AT2 cells which have doubled
157 their DNA content and arrested at the G2-phase of the cell cycle (Fig. S3D). As these dual-
158 positive cells appear an order of magnitude more rare than the AT2 binucleation rate estimated
159 in Figure 1 (e.g., < 0.2% lineage-labelled AT2 cells), we may be missing polyploidization events
160 during the AT2-to-AT1 transition, when *Sftpc*^{Cre}-expression is likely waning. Crossing the
161 *Rosa*^{Confetti}-reporter strain to a Cre-driver whose expression increases during the AT2-to-AT1
162 transition may be required to assess the full extent of alveolar epithelial polyploidization during
163 the lung injury-repair sequence. Nonetheless, these data show that lung injury can generate
164 binucleated polyploid AT2 cells (Fig. 1), and possibly polyploid mononuclear AT2 cells (Fig.
165 S3C), where polyploidization likely occurs during the post-injury, reparative phase of the
166 bleomycin model.
167
168 **Inhibiting the Integrated Stress Response attenuates AT2 hypertrophy**

To determine whether injury-induced AT2 hypertrophy and polyploidy can be inhibited or reversed, we considered small molecule approaches known to target stress-activated pathways, recently suggested to guide injured AT2 cells through their vulnerable transition towards an AT1 fate (16, 17). The integrated stress response (ISR) is a highly conserved signaling network that helps cells adapt to a range of environmental stresses, through activating kinases that inhibit bulk protein translation in favor of the translation of select mRNAs encoding transcription factors such as ATF4 that promote the transcription of molecular chaperones and other stress adaptive genes (31). A central integrator of these diverse stress-responsive kinases is the eIF2 complex, where phosphorylation of eIF2a at a single serine residue limits translation (32). In this way, eIF2a phosphorylation and its diverse downstream consequences comprise the ISR (33, 34). A small molecule integrated stress response inhibitor, ISRIB, was found to render cells insensitive to eIF2α phosphorylation, thereby restoring translation capacity to normalize cell function (35-37) and limit a range of tissue pathologies in murine disease models (38-42). Our team recently discovered that ISRIB improves fibrosis in murine models by limiting abundance of AT2 cells stalled at the AT2-to-AT1 transition state (17). Since bleomycin-injured AT2 cells show activation of ISR-associated genes (17), we reason persistent activation of the ISR in AT2 cells can thwart alveolar epithelial repair. However, particular morphogenetic features of the AT2-to-AT1 transition that drive persistence of this cell stress state remain unclear. Remarkably, we find that bleomycin-injured *Sftpc*$^{\text{Cre-ER}}$; $^{\text{Lox-Stop-Lox}}$zsGreen mice treated with ISRIB show complete inhibition of AT2 hypertrophy, and no evidence of binucleation (Fig. 6A,B). Although ISRIB did not prevent AT2 cell binucleation in *ex vivo* cell cultures, ISRIB treatment did limit the rate of binucleation, as well as formation of the largest cells, inferred from nuclear size within these cells (Fig. 6C-F). These data suggest that the AT2 hypertrophic response to injury is sensitive to inhibition of the ISR. Evidence for modest cell size attenuation in *ex vivo* AT2 cultures suggests that ISRIB may limit hypertrophic growth through an AT2 cell-autonomous mechanism.

197 **Discussion**

198 For decades, clinical pathologists have described the development of “hypertrophic” AT2 cells
199 after injury, but mechanisms that drive this state and degree to which it benefits and/or
200 constrains the lung injury-repair cycle is not known. We show that some of this hypertrophic
201 growth is associated with AT2 polyploidy, most notably binucleated AT2 cells. *Ex vivo* analysis
202 suggests the route to polyploidy is via failed cytokinesis during the AT2-to-AT1 flattening
203 process. Remarkably, attenuating the ISR with ISRIB limits the abundance of hypertrophic,
204 polyploid AT2 cells after bleomycin injury and *ex vivo* culture, suggesting the effects of ISRIB
205 may be AT2 cell-autonomous. Given recent high resolution time-series sampling of the injured
206 lung and analysis by single cell RNA-sequencing revealing that the AT2-to-AT1 transition state
207 expresses genes associated with the ISR (15), we suggest that lung injury persistently activates
208 the ISR in AT2 cells as they enlarge and flatten to repair the alveolar epithelium, increasing their
209 susceptibility to cytokinesis failure into polyploid AT2 cells. A key consequence of AT2
210 polyploidization will be loss of the AT2 stem cell daughter, which may compromise future
211 regenerative potential of alveoli served by that AT2 progenitor. We propose that attenuating the
212 ISR helps guide AT2 cells through this vulnerable cell-division/trans-differentiation
213 morphogenetic sequence without polyploidy (Fig. 7, Model).
214
215 Evidence that AT2 binucleation does not exclusively correlate with cells expressing the highest
216 levels of Krt8 protein is noteworthy. While elevated Krt8 expression is associated with an
217 aberrant AT2-to-AT1 transition state (14, 15), perhaps this transition is only one of a number of
218 transcriptionally distinct routes cells take as they repair the injured alveolar epithelium. Given
219 the increased size and presumed fragility of polyploid alveolar cells, we suspect they are
220 inadequately represented in current lung single cell RNA-sequencing pipelines. To understand
221 how these cells specifically contribute to alveolar repair, it will be necessary to revise existing
222 cell sorting pipelines to quantify the abundance and degree of alveolar epithelial polyploidy, as
223 well as isolate these cells for downstream transcriptomic analyses to establish the distinct
224 features of the polyploid cell state (26).
225
226 Recent injury-repair studies using live-imaging of zebrafish epicardium as a simple epithelial
227 model system reveal that cells along a closing wound-front manifest higher tension and rates of
228 binucleation due to failed cytokinesis (21). While one study suggests this may be due to
229 excessive integrin-based extracellular matrix adhesive tension that ultimately interferes with

230 contractility of the actin-myosin cytokinetic ring (43), whether persistent mechano-activation of
231 cell-cell adhesive junctions also contribute remains unclear.
232
233 Although bleomycin-injury leads to binucleation in only ~5% of lineage-labeled AT2 cells, total
234 alveolar epithelial cell polyploidy may be much greater, particularly given evidence for
235 mononuclear polyploidy across tissues (28). We find that injury induces a number of
236 hypertrophic, SpC-expressing cells manifesting greatly enlarged single nuclei, but newer
237 methods will be required to distinguish true mononuclear polyploidy (i.e., $\geq$4N DNA content in a
238 G_1-phase cell) from AT2 cells arrested post-genome doubling at the G_2-phase (i.e., also 4N
239 DNA content) (44). Another limitation of this study is our reliance on the DNA-damaging agent
240 bleomycin as an injury model, which could bias the alveolar repair response towards AT2
241 polyploidy. Future work will be required to determine the generality of this paradigm, and
242 whether AT2 polyploidy can be induced by other forms of injury (e.g., viral or pneumonectomy
243 model of alveologenesis).
244
245 Conceptually, it will be important address whether AT2 polyploidization is restricted to the
246 transdifferentiating daughter, sparing normal ploidy of the renewed AT2 or if lung injury
247 promotes AT2 endocycling/endomitosis, resulting in a polyploid facultative progenitor. The
248 former would generate polyploid AT1 cells, which might allow AT1 cells to become larger with
249 excess DNA copies for environmental adaptation (18). Indeed, a recent proof-of-concept study,
250 which genetically induced cytokinesis failure in AT2 cells, found that binucleation does not
251 obviously prevent trans-differentiation towards at AT1 fate (45). These data are consistent with
252 our own evidence that binucleation is compatible with expression of the AT1-marker, podoplanin
253 (Fig. 2A and 6D). Polyploidization of AT2 cells could provide extra DNA copies for surfactant
254 biosynthesis, similar to how mammary epithelial cells become polyploid during lactation to
255 maximize milk production (23). However, the induction of AT2 polyploidy would likely
256 compromise its progenitor function, which requires faithful segregation of additional
257 chromosomes during mitosis for stem cell renewal (28). Even heart tissue, which comprises
258 large binucleated cardiomyocytes suited to contractility, relies on a low percentage of
259 mononuclear diploid progenitor cells (2-14%) to drive regeneration post-injury. Mouse strains
260 with a greater percentage of these mononuclear diploid cells (14%) recover from injury faster
261 than strains with a lower percentage (2%) (46). Given this precedence, we reason that even a
262 small percentage of AT2 cells becoming polyploid during an injury event (~5% per injury) could

263 ultimately contribute to substantial loss of AT2 progenitor renewal over a lifetime, absent
264 alternate mechanisms for AT2 progenitor replacement.
265
266 It will be important to understand how alveolar epithelial cells sustain the polyploid state.
267 Forced-induction of polyploidy in retinal pigmented epithelial cells requires activation of p53
268 signaling (47). Given recent evidence that forced-activation of p53 may facilitate the AT2-to-
269 AT1 transition during lung injury (16), it is possible that induced polyploidy plays a beneficial role
270 in the earliest stages of alveolar epithelial repair. However, evidence that the integrated stress
271 response inhibitor, ISRIB, attenuates formation or duration of hypertrophic alveolar epithelial
272 cells (this study) and promotes lung repair in the bleomycin model (17), raises the possibility
273 that maintaining polyploid cells for too long may be detrimental.
274
275 The lung needs to repair in a manner that does not massively increase cell numbers (48).
276 Epithelial polyploidization post-injury may be a way to repair such tissues where excessive
277 cellularity may be problematic. Epithelial polyploidization consequent to injury is a process with
278 short-term benefits (e.g., larger cells with enhanced barrier function/reduced leak, increased
279 DNA copies for adaptation to stressful environments), but long-term consequences (e.g.,
280 reduced stem cell maintenance due to loss of self-renewed mononuclear AT2). Our data raise
281 the possibility that modulators of the ISR may be leveraged to restore AT2 progenitor function
282 during injury. Future work will be required to understand the means by which ISRIB limits
283 formation of or guides the transition of hypertrophic, polyploid AT2 cells towards an AT1
284 phenotype, and degree to which induced polyploidy contributes to alveolar epithelial cell
285 heterogeneity or adaptation in lung disease.
286
287
288
289
290
291
292
293
294
295
296
297

298 **Materials and Methods**

299

300 **Key resources Table**

REAGENT or RESOURCE	SOURCE	IDENTIFIER
Antibodies		
Rat anti-mouse I-A/I-E (MHC II), BUV395	BD Biosciences	Cat#743876, RRID:AB_2741827
Rat anti-mouse CD45, APC	BioLegend	Cat#102410
Rat anti-mouse CD31, APC	BioLegend	Cat#103112
Rat anti-mouse CD326 (Ep-CAM), PE/Cy7	BioLegend	Cat#118216
Rat anti-mouse CD11c, PE/Cy7	BioLegend	Cat#117318
Propidium Iodide	ThermoFisher Scientific	Cat#P1304MP
Biotin Rat Anti-mouse CD16/32	BD Biosciences	Cat#553143
Biotin Rat Anti-mouse TER119/Erythroid Cells	BD Biosciences	Cat#553672
Biotin Rat Anti-mouse CD45	BD Biosciences	Cat#553078
Biotin Rat Anti-mouse CD90	BD Biosciences	Cat#554896
Anti-Prosurfactant Protein C (proSP-C)	Millipore Sigma	Cat#AB3786
Anti-β-catenin	Millipore Sigma	Cat#06-734
Anti-β-catenin	BD Biosciences	Cat#610153
Podoplanin	DSHB (University of Iowa)	Cat#8.1.1, RRID:AB_531893
Krt8	DSHB (University of Iowa)	Cat#TROMA-I, RRID:AB_531826
Alexa Fluro 680 Phalloidin	Invitrogen	Cat#A22286
Goat anti-rabbit Alexa Fluor 488	Invitrogen	Cat#A11008
Goat anti-mouse Alexa Fluor 568	Invitrogen	Cat#A11004
Goat anti-hamster Alexa Fluor 594	Invitrogen	Cat#A21113
Goat anti-rat Alexa Fluor 546	Invitrogen	Cat#A11081
Chemicals, Peptides, and Recombinant Proteins		
Bleomycin	Fresenius Kabi	Cat#0703-3154-01
0.9% saline chloride	BBraun	Cat#R5201-01
ISRIB	AdooQ BioScience	Cat#A14302
Tamoxifen	Sigma	Cat#T5648
Corn oil	Sigma	Cat#C8267
Vybrant DyeCycle Violet Stain	Invitrogen	Cat#V35003
Hoechst 33342	ThermoFisher Scientific	Cat#62249
Draq5	ThermoFisher Scientific	Cat#62251
ROCK1 inhibitor Y-27632	Selleckhem	S1049
ProLong Gold Antifade Mountant	ThermoFisher Scientific	Cat#P36934
Eriochrome black	Sigma	Cat#E2377
CD326 (EpCAM) Microbeads, mouse	Miltenyi Biotec	Cat#130-105-958
Matrigel	Corning	Cat#356231
Collagenase	Millipore Sigma	Cat#C0130
Elastase	Worthington	Cat#LS002292

Deoxyribonuclease (DNase) I	Sigma	Cat#D4513
Dispase	Corning	Cat#47743-724
PharmLyse (Red Blood Cell Lysis)	BD Biosciences	Cat#555899
Purified Rat Anti-mouse CD16/CD32 (Mouse FcBlock)	BD Biosciences	Cat#553142
Streptavidin MagneSphere Paramagnetic Particles	Promega	Cat#Z548C
Mouse CD45 MicroBeads	Miltenyi Biotec	Cat#130-052-301
autoMACS Running Buffer – MACS Separation	Miltenyi Biotec	Cat#130-091-221
Critical Commercial Assays		
SHIELD	LifeCanvas Technologies	Cat#EI-Z1001,#SH-BS,#SH-ES,#SH-ON
MultiMACS Cell24 Separator	Miltenyi Biotec	
Experimental Models: Organisms/Strains		
Mouse: C57BL/6J (8-12 weeks old)	The Jackson Laboratory	JAX: 000664
Mouse: *Sftpc*^{CreER}	The Jackson Laboratory	JAX: 020940
Mouse: R26R^{ZsGreen}	The Jackson Laboratory	JAX: 007906
Mouse: *Sftpc*^{CreER}	International Mouse Strain Resource	MGI: 5444645
Mouse: R26R^{eYFP}	The Jackson Laboratory	JAX: 006148
Mouse: R26R^{Confetti}	The Jackson Laboratory	JAX: 013731
Software and Algorithms		
FIJI/ImageJ (version: 2.1.0/1.53c)	Schneider, CA et al., 2012	https://imagej.nih.gov/ij/
Stardist plugin	Schmit, U et al., 2018	Cell/nuclear size quantification https://arxiv.org/abs/1806.03535
Other		
Vibratome	Leica Microsystems	VT1200s
Cryostat	Reichert-Jung	Cryocut 1800
W1 Spinning Disk Confocal	Nikon Instruments	
BioStation CT or other	Nikon Instruments	
Axioplan2 epifluorescence microscope	Zeiss; 20x objective (Air)	AxioCAM HR Camera with AxioVision 4.8 software
A1R Confocal	Nikon Instruments	

301

302

303 **Methods Details**

304 **Mice:** C57BL/6 mice were obtained from Jackson laboratories (Jax stock 000664). *Sftpc*^{CreER}
305 (49), Ai6-R26^{zsGreen}, *Sftpc*$^{CreERT2;R26ReYFP}$ (kindly provided by Ed Morrisey, University of
306 Pennsylvania)(50, 51) and *Sftpc*$^{CreER;R26R\text{-}Confetti}$ (8) (Jax stocks 028054, 007906, 006148,
307 013731). Only male mice were used in bleomycin-injury experiments based on established
308 injury severity in males relative to females, which improves dynamic range of assays for
309 comparisons (52). Eight to twelve week old mice were used as young adult mice. All
310 experimental protocols were approved by the Institutional Animal Care and Use Committee at
311 Northwestern University (Chicago, IL, USA). All strains including wildtype mice are bred and
312 housed at a barrier- and pathogen-free facility at the Center for Comparative Medicine at
313 Northwestern University.
314

315 **Cre recombination, bleomycin administration, ISRIB administration**

316 For nuclear activation of Cre-ER, tamoxifen was dissolved in sterile corn oil at 10 mg/100μL and
317 administered via oral gavage once a day for two days to induce Cre-recombination of floxed
318 alleles for lineage-tracing. For bleomycin injury, mice were anesthetized and intubated prior to
319 the intratracheal administration of bleomycin (0.025 units in 50μL 0.9% saline). Lungs were
320 harvested at indicated time points for downstream analyses (e.g., fixation and frozen sectioning
321 for immunofluorescence analysis, AT2 cell isolation by negative selection (53) or EpCam+
322 selection (54) and flow cytometry methods (17, 55) with modifications (below). ISRIB (AdooQ
323 BioScience, A14302) was first reconstituted in DMSO to the concentration 4mg/mL and then
324 further diluted using PBS to a final concentration of 0.3125 mg/mL (56). ISRIB was prepared at
325 2.5 mg/kg and administered daily through intraperitoneal injection in a volume of 200μL. Control
326 animals were treated with vehicle (DMSO/PBS) alone.
327

328 **Tissue preparation, AT2 isolation, flow cytometry and sorting:** Tissue preparation for AT2
329 isolation and analyses was performed as described (17, 55), with modifications. Briefly, mice
330 were euthanized and lungs were perfused through the right ventricle with 10ml of HBSS. Lungs
331 were removed and infiltrated with dispase and 0.2 mg/ml DNase I dissolved in HBSS with Ca^{2+}
332 and Mg^{2+}, using syringe with 30G needle. Lungs were chopped with scissors and incubated in
333 DMEM containing 5% FBS for 45 minutes with agitation. The tissue suspension was filtered
334 through a 70 μM strainer and washed in 10 mL media (DMEM; 5% FBS). The pellet was then
335 suspended in red blood cell (RBC) lysis buffer for 1 minute, washed with media, and filtered
336 through 40 μM strainer. The cells were incubated with EpCAM magnetic beads and AT2 were

337 collected using the MultiMACS Cell24 Separator (Miltenyi Biotec). Automated cell counting was
338 performed using Nexcelom K2 Cellometer with AO/PI reagent. Cells were incubated with
339 FcBlock (BD Biosciences, San Jose, California), and stained with a mixture of fluorochrome-
340 conjugated antibodies, as listed above. DNA content was quantified using Vybrant DyeCycle
341 Violet. Single color controls were prepared using BD CompBeads (BD Biosciences, San Jose,
342 California) and Arc beads (Invitrogen, Waltham, Massachusetts). Flow cytometry and cell
343 sorting were performed at the Northwestern University Robert H. Lurie Comprehensive Cancer
344 Center Flow Cytometry Core facility (Chicago, Illinois). Data were acquired on a custom BD
345 FACSymphony instrument using BD FACSDiva software (BD Biosciences, San Jose,
346 California). Compensation and analysis were performed using FlowJo software (TreeStar). Each
347 cell population was identified using sequential gating strategy. The percentage of cells in the
348 live/singlets gate was multiplied by the number of live cells using Cellometer K2 Image
349 cytometer to obtain cell counts. Cell sorting was performed using BD FACSAria III instrument
350 using 100μm nozzle and 40 psi pressure. *Cytospin*: Following AT2 sorting, collected cells were
351 spun at 300g for 10 minutes. Following resuspension in PBS, cells were plated onto slides.
352 Slides were spun in cytospin filters at 100g for 5 minutes followed by staining with phalloidin
353 (1:50) and Hoescht (1:10,000).
354
355 **AT2 isolation for ex vivo two-dimensional culture:** Lungs were inflated intratracheally with
356 Dispase and incubated for 45 minutes with agitation. Lungs were chopped and incubated in
357 7mL of media containing 10% FBS and DNase I (1 mg/mL) for 10 minutes. Tissue suspensions
358 were filtered through a 70μM strainer. The cell pellets were resuspended in RBC lysis buffer for
359 2 minutes. Alveolar epithelial cells were enriched through negative selection against biotinylated
360 CD16/32, CD45, CD90, and TER119 antibodies. The cell suspensions were then incubated at
361 37°C for 2 hours followed by gentle panning. Cells were counted and cultured in complete
362 media (10% FBS, 2% Penicillin and Streptomycin) onto 12mm glass coverslips. Starting 48
363 hours after isolation, cells received a daily media change either containing 0.025μM ISRIB or
364 DMSO. Cell samples were pooled from 3 mice. Rat AT2 cells were collected as previously
365 described (57).
366
367 **AT2 organoid culture**: For organoid culture, cells were prepared as previously described (8)
368 with modifications. Mice received tamoxifen 14 days prior to isolation. AT2 isolation was
369 conducted as described above. For fibroblast isolation, lungs were inflated with 1 mL of
370 collagenase (200 U/mL), elastase (4 U/mL), and DNase solution (0.25 mg/mL). Lungs were cut

371 into pieces and incubated for 30 minutes at 37°C in digestion buffer. Lungs were processed in
372 C-tubes (Miltenyi Biotec, 130-093-237) using GentleMACS/OctoMACS dissociator (Miltenyi
373 Biotec). Suspensions were filtered through 40 μM strainer and rinsed with MACS buffer. The
374 pellet was resuspended in RBC lysis buffer, washed with MACS, and incubated with CD45
375 magnetic beads to deplete CD45+ cells. CD45- cell fraction was collected using the MultiMACS
376 Cell24 Separator (Miltenyi Biotec). Cells were sorted as described above. Following sorting,
377 $5x10^3$ zsGreen+ AT2 were mixed with $5x10^4$ fibroblasts in 50% Matrigel (Corning, 356231) and
378 50% organoid media (αMEM, penicillin/streptomycin, insulin/transferrin/selenium, FBS, heparin,
379 Amphotericin B, Rock1 inhibitor, L-glutamine) in 0.4 μM Transwell inserts. Cell/Matrigel mixtures
380 were solidified at 37°C for 5 minutes before 300μl of media was added under the Transwell. 24
381 hours after isolation, organoids received media change every other day containing either 1 μM
382 ISRIB or DMSO for 10 days.
383
384 **Tissue sectioning, immunofluorescence and image analysis:** After euthanasia and
385 perfusion, trachea was cannulated with Luer syringe stub blunt needle and mouse lungs were
386 inflated with 4% paraformaldehyde at 15 cm H_2O column pressure. Lungs were fixed in 4%
387 paraformaldehyde (PFA) overnight at 4°C followed by cryo-embedding in optimal cutting-
388 temperature compound (OCT). Sections were cut at 14μM on a cryo-vibratome. For
389 immunostaining, sections were blocked in 10% normal goat serum (NGS), 0.3%TritonX-100 in
390 PBS for 30 minutes followed by an additional 1:10 anti-mouse Fab (H+L) for 2 hours. Primary
391 antibodies were prepared in 2% NGS 0.3%TritonX-100 PBS and applied to sections overnight
392 at 4°C. Sections were washed in PBS followed by secondary antibodies for 30 minutes. Lastly,
393 sections were incubated in Hoechst (1:10,000) for 5 minutes followed by a brief incubation of
394 0.3% Eriochrome black prior to mounting. Primary antibodies were used at concentrations
395 described below. *For 2D culture*, cells were fixed 4 days after isolation in 4% PFA. For the
396 alveolar organoids, organoids were fixed 10 days after isolation. Fixed cells and organoids were
397 neutralized in 10 mM glycine followed by blocking in 10% normal goat serum (NGS) in
398 0.3%TritonX-100 PBS. Primary antibodies were prepared in 3% NGS in 0.3%TritonX-100 PBS
399 and applied for 1 hour at room temperature. Following PBS washes, fluorophore-conjugated
400 secondary antibodies were prepared at 1:300 for 30 minutes in the dark at room temperature.
401 Hoechst was diluted 1:10,000 and applied for 5 minutes at room temperature following
402 secondary antibody incubation. Coverslips and filters were mounted using ProLong Gold anti-
403 fade solution. Images were obtained using Zeiss Axioplan epifluorescence and Nikon W1

404 Spinning Disk confocal microscopes. *For nuclear area quantification*, 5 fields of view were
405 selected for each condition per biological replicate. Images were taken on a Zeiss microscope
406 and analyzed in Fiji using the Stardist plugin. Primary antibodies were as follows: SFTPC
407 (1:100); beta-catenin (1:100); Podoplanin (1:30); Krt8 (1:30), and F-actin (1:50). *For thick*
408 *section imaging with tissue clearing*, lungs were sliced in PBS using a vibratome (Leica
409 VT1200s) in 200μm thick sections. Tissue slices were cleared using the LifeCanvas
410 Technologies SHIELD method (Cambridge, MA, USA).
411
412 **Live-cell imaging:** Freshly isolated alveolar epithelial cells were plated at 500K/well in a 12 well
413 plate. 48 hours post-isolation, media was changed and adherent cells were imaged every 15-
414 minutes on a Biostation-CT system (Nikon Instruments, New York, USA) for a total of 5 hours.
415 Image sequences were analyzed in Fiji (ImageJ v: 2.1.0/1.53c).
416
417 **Statistical analysis:** Data analysis and statistical tests were performed using GraphPad Prism
418 software (v.9.2.0).
419

References

1. Bharat A, Querrey M, Markov NS, Kim S, Kurihara C, Garza-Castillon R, Manerikar A, Shilatifard A, Tomic R, Politanska Y, Abdala-Valencia H, Yeldandi AV, Lomasney JW, Misharin AV, Budinger GRS. Lung transplantation for patients with severe COVID-19. *Sci Transl Med* 2020; 12.
2. Bharat A, Querrey M, Markov NS, Kim S, Kurihara C, Garza-Castillon R, Manerikar A, Shilatifard A, Tomic R, Politanska Y, Abdala-Valencia H, Yeldandi AV, Lomasney JW, Misharin AV, Budinger GRS. Lung transplantation for pulmonary fibrosis secondary to severe COVID-19. *medRxiv* 2020.
3. Spagnolo P, Balestro E, Aliberti S, Cocconcelli E, Biondini D, Casa GD, Sverzellati N, Maher TM. Pulmonary fibrosis secondary to COVID-19: a call to arms? *Lancet Respir Med* 2020; 8: 750-752.
4. Chen J, Wu H, Yu Y, Tang N. Pulmonary alveolar regeneration in adult COVID-19 patients. *Cell Res* 2020; 30: 708-710.
5. Delorey TM, Ziegler CGK, Heimberg G, Normand R, Yang Y, Segerstolpe A, Abbondanza D, Fleming SJ, Subramanian A, Montoro DT, Jagadeesh KA, Dey KK, Sen P, Slyper M, Pita-Juarez YH, Phillips D, Biermann J, Bloom-Ackermann Z, Barkas N, Ganna A, Gomez J, Melms JC, Katsyv I, Normandin E, Naderi P, Popov YV, Raju SS, Niezen S, Tsai LT, Siddle KJ, Sud M, Tran VM, Vellarikkal SK, Wang Y, Amir-Zilberstein L, Atri DS, Beechem J, Brook OR, Chen J, Divakar P, Dorceus P, Engreitz JM, Essene A, Fitzgerald DM, Fropf R, Gazal S, Gould J, Grzyb J, Harvey T, Hecht J, Hether T, Jane-Valbuena J, Leney-Greene M, Ma H, McCabe C, McLoughlin DE, Miller EM, Muus C, Niemi M, Padera R, Pan L, Pant D, Pe'er C, Pfiffner-Borges J, Pinto CJ, Plaisted J, Reeves J, Ross M, Rudy M, Rueckert EH, Siciliano M, Sturm A, Todres E, Waghray A, Warren S, Zhang S, Zollinger DR, Cosimi L, Gupta RM, Hacohen N, Hibshoosh H, Hide W, Price AL, Rajagopal J, Tata PR, Riedel S, Szabo G, Tickle TL, Ellinor PT, Hung D, Sabeti PC, Novak R, Rogers R, Ingber DE, Jiang ZG, Juric D, Babadi M, Farhi SL, Izar B, Stone JR, Vlachos IS, Solomon IH, Ashenberg O, Porter CBM, Li B, Shalek AK, Villani AC, Rozenblatt-Rosen O, Regev A. COVID-19 tissue atlases reveal SARS-CoV-2 pathology and cellular targets. *Nature* 2021.
6. McDonald LT. Healing after COVID-19: are survivors at risk for pulmonary fibrosis? *American journal of physiology* 2021; 320: L257-L265.
7. Rock JR, Hogan BL. Epithelial progenitor cells in lung development, maintenance, repair, and disease. *Annual review of cell and developmental biology* 2011; 27: 493-512.
8. Barkauskas CE, Cronce MJ, Rackley CR, Bowie EJ, Keene DR, Stripp BR, Randell SH, Noble PW, Hogan BL. Type 2 alveolar cells are stem cells in adult lung. *The Journal of clinical investigation* 2013; 123: 3025-3036.
9. Aso Y, Yoneda K, Kikkawa Y. Morphologic and biochemical study of pulmonary changes induced by bleomycin in mice. *Lab Invest* 1976; 35: 558-568.
10. Miller BE, Hoo KG. Regulation of phosphatidylcholine biosynthesis in activated alveolar type II cells. *American journal of respiratory cell and molecular biology* 1989; 1: 127-136.
11. Miller BE, Hook GE. Hypertrophy and hyperplasia of alveolar type II cells in response to silica and other pulmonary toxicants. *Environ Health Perspect* 1990; 85: 15-23.
12. Kasper M, Haroske G. Alterations in the alveolar epithelium after injury leading to pulmonary fibrosis. *Histol Histopathol* 1996; 11: 463-483.
13. Wu H, Yu Y, Huang H, Hu Y, Fu S, Wang Z, Shi M, Zhao X, Yuan J, Li J, Yang X, Bin E, Wei D, Zhang H, Zhang J, Yang C, Cai T, Dai H, Chen J, Tang N. Progressive Pulmonary Fibrosis Is Caused by Elevated Mechanical Tension on Alveolar Stem Cells. *Cell* 2020; 180: 107-121 e117.

14. Jiang P, Gil de Rubio R, Hrycaj SM, Gurczynski SJ, Riemondy KA, Moore BB, Omary MB, Ridge KM, Zemans RL. Ineffectual AEC2-to-AEC1 Differentiation in IPF: Persistence of KRT8(hi) Transitional State. *American journal of respiratory and critical care medicine* 2020; 201: 1443-1447.
15. Strunz M, Simon LM, Ansari M, Kathiriya JJ, Angelidis I, Mayr CH, Tsidiridis G, Lange M, Mattner LF, Yee M, Ogar P, Sengupta A, Kukhtevich I, Schneider R, Zhao Z, Voss C, Stoeger T, Neumann JHL, Hilgendorff A, Behr J, O'Reilly M, Lehmann M, Burgstaller G, Konigshoff M, Chapman HA, Theis FJ, Schiller HB. Alveolar regeneration through a Krt8+ transitional stem cell state that persists in human lung fibrosis. *Nat Commun* 2020; 11: 3559.
16. Kobayashi Y, Tata A, Konkimalla A, Katsura H, Lee RF, Ou J, Banovich NE, Kropski JA, Tata PR. Persistence of a regeneration-associated, transitional alveolar epithelial cell state in pulmonary fibrosis. *Nature cell biology* 2020; 22: 934-946.
17. Watanabe S, Markov NS, Lu Z, Piseaux Aillon R, Soberanes S, Runyan CE, Ren Z, Grant RA, Maciel M, Abdala-Valencia H, Politanska Y, Nam K, Sichizya L, Kihshen HG, Joshi N, McQuattie-Pimentel AC, Gruner KA, Jain M, Sznajder JI, Morimoto RI, Reyfman PA, Gottardi CJ, Budinger GRS, Misharin AV. Resetting proteostasis with ISRIB promotes epithelial differentiation to attenuate pulmonary fibrosis. *Proc Natl Acad Sci U S A* 2021; 118.
18. Schoenfelder KP, Fox DT. The expanding implications of polyploidy. *J Cell Biol* 2015; 209: 485-491.
19. Amodeo AA, Skotheim JM. Cell-Size Control. *Cold Spring Harb Perspect Biol* 2016; 8: a019083.
20. Cohen E, Allen SR, Sawyer JK, Fox DT. Fizzy-Related dictates A cell cycle switch during organ repair and tissue growth responses in the Drosophila hindgut. *Elife* 2018; 7.
21. Cao J, Wang J, Jackman CP, Cox AH, Trembley MA, Balowski JJ, Cox BD, De Simone A, Dickson AL, Di Talia S, Small EM, Kiehart DP, Bursac N, Poss KD. Tension Creates an Endoreplication Wavefront that Leads Regeneration of Epicardial Tissue. *Dev Cell* 2017; 42: 600-615 e604.
22. Herrtwich L, Nanda I, Evangelou K, Nikolova T, Horn V, Sagar, Erny D, Stefanowski J, Rogell L, Klein C, Gharun K, Follo M, Seidl M, Kremer B, Munke N, Senges J, Fliegauf M, Aschman T, Pfeifer D, Sarrazin S, Sieweke MH, Wagner D, Dierks C, Haaf T, Ness T, Zaiss MM, Voll RE, Deshmukh SD, Prinz M, Goldmann T, Holscher C, Hauser AE, Lopez-Contreras AJ, Grun D, Gorgoulis V, Diefenbach A, Henneke P, Triantafyllopoulou A. DNA Damage Signaling Instructs Polyploid Macrophage Fate in Granulomas. *Cell* 2016; 167: 1264-1280 e1218.
23. Rios AC, Fu NY, Jamieson PR, Pal B, Whitehead L, Nicholas KR, Lindeman GJ, Visvader JE. Essential role for a novel population of binucleated mammary epithelial cells in lactation. *Nat Commun* 2016; 7: 11400.
24. Wang J, Batourina E, Schneider K, Souza S, Swayne T, Liu C, George CD, Tate T, Dan H, Wiessner G, Zhuravlev Y, Canman JC, Mysorekar IU, Mendelsohn CL. Polyploid Superficial Cells that Maintain the Urothelial Barrier Are Produced via Incomplete Cytokinesis and Endoreplication. *Cell Rep* 2018; 25: 464-477 e464.
25. Quinton RJ, DiDomizio A, Vittoria MA, Kotynkova K, Ticas CJ, Patel S, Koga Y, Vakhshoorzadeh J, Hermance N, Kuroda TS, Parulekar N, Taylor AM, Manning AL, Campbell JD, Ganem NJ. Whole-genome doubling confers unique genetic vulnerabilities on tumour cells. *Nature* 2021; 590: 492-497.
26. Fox DT, Soltis DE, Soltis PS, Ashman TL, Van de Peer Y. Polyploidy: A Biological Force From Cells to Ecosystems. *Trends Cell Biol* 2020; 30: 688-694.
27. Gjelsvik KJ, Besen-McNally R, Losick VP. Solving the Polyploid Mystery in Health and Disease. *Trends Genet* 2019; 35: 6-14.

520 28. Ovrebo JI, Edgar BA. Polyploidy in tissue homeostasis and regeneration. *Development*
521 2018; 145.
522 29. Matsumoto T, Wakefield L, Tarlow BD, Grompe M. In Vivo Lineage Tracing of Polyploid
523 Hepatocytes Reveals Extensive Proliferation during Liver Regeneration. *Cell Stem Cell*
524 2020; 26: 34-47 e33.
525 30. Nabhan AN, Brownfield DG, Harbury PB, Krasnow MA, Desai TJ. Single-cell Wnt signaling
526 niches maintain stemness of alveolar type 2 cells. *Science* 2018; 359: 1118-1123.
527 31. Emanuelli G, Nassehzadeh-Tabriz N, Morrell NW, Marciniak SJ. The integrated stress
528 response in pulmonary disease. *Eur Respir Rev* 2020; 29.
529 32. Sudhakar A, Ramachandran A, Ghosh S, Hasnain SE, Kaufman RJ, Ramaiah KV.
530 Phosphorylation of serine 51 in initiation factor 2 alpha (eIF2 alpha) promotes complex
531 formation between eIF2 alpha(P) and eIF2B and causes inhibition in the guanine
532 nucleotide exchange activity of eIF2B. *Biochemistry* 2000; 39: 12929-12938.
533 33. Pakos-Zebrucka K, Koryga I, Mnich K, Ljujic M, Samali A, Gorman AM. The integrated
534 stress response. *EMBO Rep* 2016; 17: 1374-1395.
535 34. Costa-Mattioli M, Walter P. The integrated stress response: From mechanism to disease.
536 *Science* 2020; 368.
537 35. Sidrauski C, McGeachy AM, Ingolia NT, Walter P. The small molecule ISRIB reverses the
538 effects of eIF2alpha phosphorylation on translation and stress granule assembly. *Elife*
539 2015; 4.
540 36. Sidrauski C, Tsai JC, Kampmann M, Hearn BR, Vedantham P, Jaishankar P, Sokabe M,
541 Mendez AS, Newton BW, Tang EL, Verschueren E, Johnson JR, Krogan NJ, Fraser CS,
542 Weissman JS, Renslo AR, Walter P. Pharmacological dimerization and activation of the
543 exchange factor eIF2B antagonizes the integrated stress response. *Elife* 2015; 4:
544 e07314.
545 37. Zyryanova AF, Kashiwagi K, Rato C, Harding HP, Crespillo-Casado A, Perera LA,
546 Sakamoto A, Nishimoto M, Yonemochi M, Shirouzu M, Ito T, Ron D. ISRIB Blunts the
547 Integrated Stress Response by Allosterically Antagonising the Inhibitory Effect of
548 Phosphorylated eIF2 on eIF2B. *Mol Cell* 2021; 81: 88-103 e106.
549 38. Anand AA, Walter P. Structural insights into ISRIB, a memory-enhancing inhibitor of the
550 integrated stress response. *FEBS J* 2020; 287: 239-245.
551 39. Chou A, Krukowski K, Jopson T, Zhu PJ, Costa-Mattioli M, Walter P, Rosi S. Inhibition of the
552 integrated stress response reverses cognitive deficits after traumatic brain injury. *Proc*
553 *Natl Acad Sci U S A* 2017; 114: E6420-E6426.
554 40. Krukowski K, Nolan A, Frias ES, Boone M, Ureta G, Grue K, Paladini M-S, Elizarraras E,
555 Delgado L, Bernales S, Walter P, Rosi S. Small molecule cognitive enhancer reverses
556 age-related memory decline in mice. *bioRxiv* 2020: 2020.2004.2013.039677.
557 41. Rabouw HH, Langereis MA, Anand AA, Visser LJ, de Groot RJ, Walter P, van Kuppeveld
558 FJM. Small molecule ISRIB suppresses the integrated stress response within a defined
559 window of activation. *Proc Natl Acad Sci U S A* 2019; 116: 2097-2102.
560 42. Watanabe S, Markov NS, Lu Z, Aillon RP, Soberanes S, Runyan CE, Ren Z, Grant RA,
561 Maciel M, Abdala-Valencia H, Politanska Y, Nam K, Sichizya L, Kihshen HG, Joshi N,
562 McQuattie-Pimentel AC, Morimoto RI, Reyfman PA, Budinger GRS, Misharin AV.
563 Resetting proteostasis with ISRIB prevents pulmonary fibrosis. *bioRxiv* 2020:
564 2020.2002.2026.965566.
565 43. Uroz M, Garcia-Puig A, Tekeli I, Elosegui-Artola A, Abenza JF, Marin-Llaurado A, Pujals S,
566 Conte V, Albertazzi L, Roca-Cusachs P, Raya A, Trepat X. Traction forces at the
567 cytokinetic ring regulate cell division and polyploidy in the migrating zebrafish
568 epicardium. *Nat Mater* 2019; 18: 1015-1023.
569 44. Zielke N, Edgar BA. FUCCI sensors: powerful new tools for analysis of cell proliferation.
570 *Wiley Interdiscip Rev Dev Biol* 2015; 4: 469-487.

571 45. Liberti DC, Kremp MM, Liberti WA, 3rd, Penkala IJ, Li S, Zhou S, Morrisey EE. Alveolar
572 epithelial cell fate is maintained in a spatially restricted manner to promote lung
573 regeneration after acute injury. *Cell Rep* 2021; 35: 109092.
574 46. Patterson M, Barske L, Van Handel B, Rau CD, Gan P, Sharma A, Parikh S, Denholtz M,
575 Huang Y, Yamaguchi Y, Shen H, Allayee H, Crump JG, Force TI, Lien CL, Makita T,
576 Lusis AJ, Kumar SR, Sucov HM. Frequency of mononuclear diploid cardiomyocytes
577 underlies natural variation in heart regeneration. *Nat Genet* 2017; 49: 1346-1353.
578 47. Potapova TA, Seidel CW, Box AC, Rancati G, Li R. Transcriptome analysis of tetraploid
579 cells identifies cyclin D2 as a facilitator of adaptation to genome doubling in the presence
580 of p53. *Mol Biol Cell* 2016; 27: 3065-3084.
581 48. Leach JP, Morrisey EE. Repairing the lungs one breath at a time: How dedicated or
582 facultative are you? *Genes Dev* 2018; 32: 1461-1471.
583 49. Rock JR, Barkauskas CE, Cronce MJ, Xue Y, Harris JR, Liang J, Noble PW, Hogan BL.
584 Multiple stromal populations contribute to pulmonary fibrosis without evidence for
585 epithelial to mesenchymal transition. *Proc Natl Acad Sci U S A* 2011; 108: E1475-1483.
586 50. Zacharias WJ, Frank DB, Zepp JA, Morley MP, Alkhaleel FA, Kong J, Zhou S, Cantu E,
587 Morrisey EE. Regeneration of the lung alveolus by an evolutionarily conserved epithelial
588 progenitor. *Nature* 2018; 555: 251-255.
589 51. Chapman HA, Li X, Alexander JP, Brumwell A, Lorizio W, Tan K, Sonnenberg A, Wei Y, Vu
590 TH. Integrin alpha6beta4 identifies an adult distal lung epithelial population with
591 regenerative potential in mice. *The Journal of clinical investigation* 2011; 121: 2855-
592 2862.
593 52. Redente EF, Jacobsen KM, Solomon JJ, Lara AR, Faubel S, Keith RC, Henson PM,
594 Downey GP, Riches DW. Age and sex dimorphisms contribute to the severity of
595 bleomycin-induced lung injury and fibrosis. *American journal of physiology* 2011; 301:
596 L510-518.
597 53. Chen J, Chen Z, Narasaraju T, Jin N, Liu L. Isolation of highly pure alveolar epithelial type I
598 and type II cells from rat lungs. *Lab Invest* 2004; 84: 727-735.
599 54. Jansing NL, McClendon J, Kage H, Sunohara M, Alvarez JR, Borok Z, Zemans RL. Isolation
600 of Rat and Mouse Alveolar Type II Epithelial Cells. *Methods Mol Biol* 2018; 1809: 69-82.
601 55. Misharin AV, Morales-Nebreda L, Mutlu GM, Budinger GR, Perlman H. Flow cytometric
602 analysis of macrophages and dendritic cell subsets in the mouse lung. *American journal
603 of respiratory cell and molecular biology* 2013; 49: 503-510.
604 56. Halliday M, Radford H, Sekine Y, Moreno J, Verity N, le Quesne J, Ortori CA, Barrett DA,
605 Fromont C, Fischer PM, Harding HP, Ron D, Mallucci GR. Partial restoration of protein
606 synthesis rates by the small molecule ISRIB prevents neurodegeneration without
607 pancreatic toxicity. *Cell Death Dis* 2015; 6: e1672.
608 57. Flozak AS, Lam AP, Russell S, Jain M, Peled ON, Sheppard KA, Beri R, Mutlu GM,
609 Budinger GR, Gottardi CJ. Beta-catenin/T-cell factor signaling is activated during lung
610 injury and promotes the survival and migration of alveolar epithelial cells. *J Biol Chem*
611 2010; 285: 3157-3167.
612

613

614

Acknowledgements

This work relied on the following Northwestern University services and core facilities: Flow Cytometry (NCI CA060553, 1S10OD011996, 1S10OD026814); Center for Advanced Microscopy (NCI CCSG P30 CA060553, NCRR 1S10 RR031680, 1S10OD021704); BioCryo facility of Northwestern University's NUANCE Center (NSF ECCS-2025633, DMR-1720139).

Funding: MH is supported by AR073270, AM is supported by HL135124, HL153312, AG049665 and AI135964; GRSB is supported by ES13995, HL071643, AG049665; CJG is supported by HL134800, AR073270 and GM129312. All authors declare no competing financial interests.

Author contributions: AW, MMH, SW, ASF, LW and RPA designed and conducted experiments; AW, MMH, ASF, AM and CJG analyzed results; RG wrote a macro for image analysis; AM advised and analyzed flow cytometry, SH, LD, MH, AM, GRSB advised and discussed results; CJG designed and supervised study, performed analysis and wrote manuscript. MH, AM, GRSB and CJG provided funding for project.

631 **Figures**

632

633 **Figure 1**: **Lung injury induces AT2 cell hypertrophy.** (**A**) Schematic of experimental design.
634 Young adult *Sftpc*^{CreER}; Lox-Stop-Lox^{ZsGreen} mice (3-5 months) received 10mg of tamoxifen via
635 oral gavage 22 days prior to administration of bleomycin (0.025 units, i.t.). Lungs from saline
636 (control) and bleomycin-treated mice were harvested on Day 10, fixed and processed for frozen
637 sectioning and immunofluorescence analysis. (**B**) Representative lung sections showing native
638 GFP fluorescence from AT2-lineage label and immunofluorescence staining of AT1 cells by
639 podoplanin (Pdpn, magenta). Scale bar = 50μm. Note lineage-labeled AT2 cells appear larger
640 after bleomycin injury. (**C**) Graph shows quantification of AT2 cell area and perimeter using
641 image analysis in FIJI (workflow in Fig. S1A). Data points are from two mice, 5 fields of view per
642 condition. Mean +/- SD. $p < 0.0001$ by t-test. To ensure robustness and increase N's, injury-
643 induced cell size increase also validated by flow cytometry in Fig. S2.

644

645

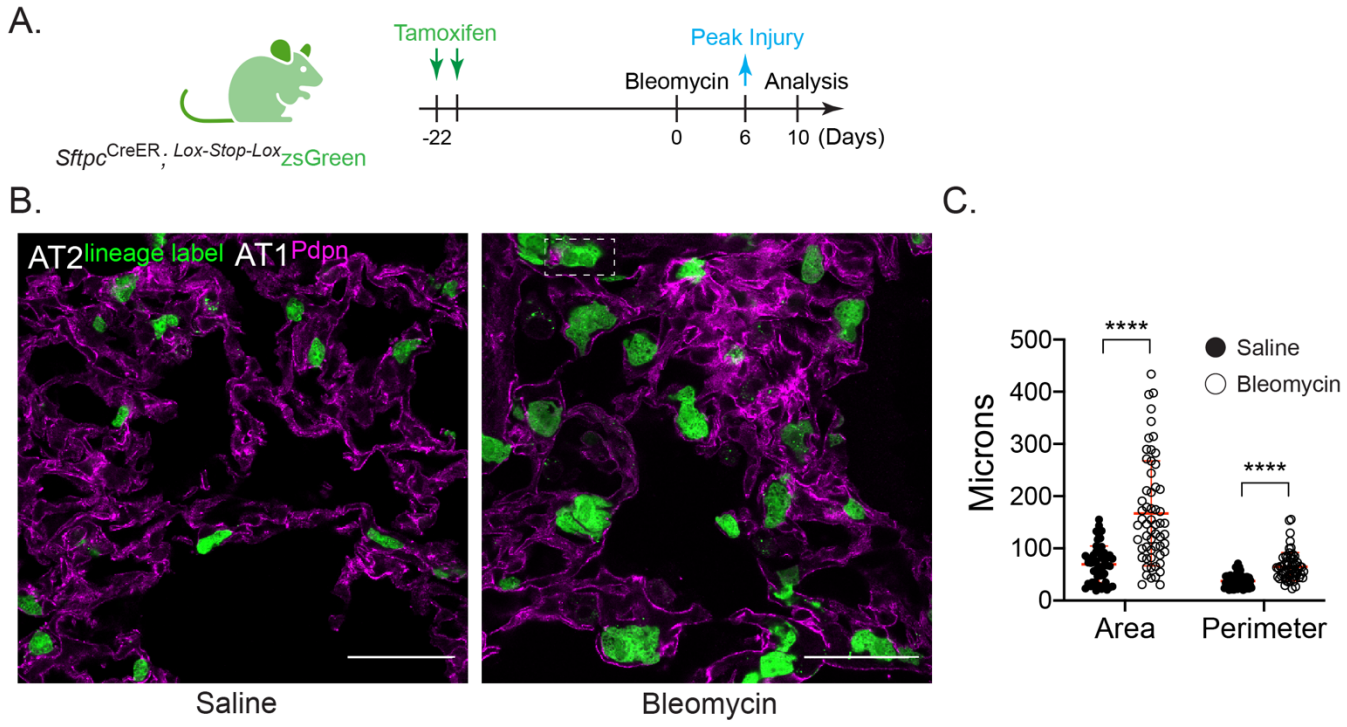

646

647 **Figure S1**: **AT2 cell hypertrophy by frozen- and thick-section image analysis**. (**A**) Black
648 and white mask of images in Figure 1 for quantification of lineage-labelled AT2 cell area and
649 perimeter (black objects, green arrow). (**B**) Injury-induced AT2 hypertrophy readily observed by
650 frozen sections, which are ~4-fold thicker than typical paraffin sections. (**C**) Hypertrophic AT2
651 phenotype is not an artefact of lineage-labeling AT2 cells. Confocal image of Vibratome-cut
652 200μm thick lung section from a C57BL/6 mouse with clearing (SHIELD method)
653 immunofluorescence detection of SpC (red) and nuclei (Draq5; cyan). Note bleomycin-treated
654 AT2 cells are clearly larger, even 21 days post-bleomycin instillation.
655
656
657

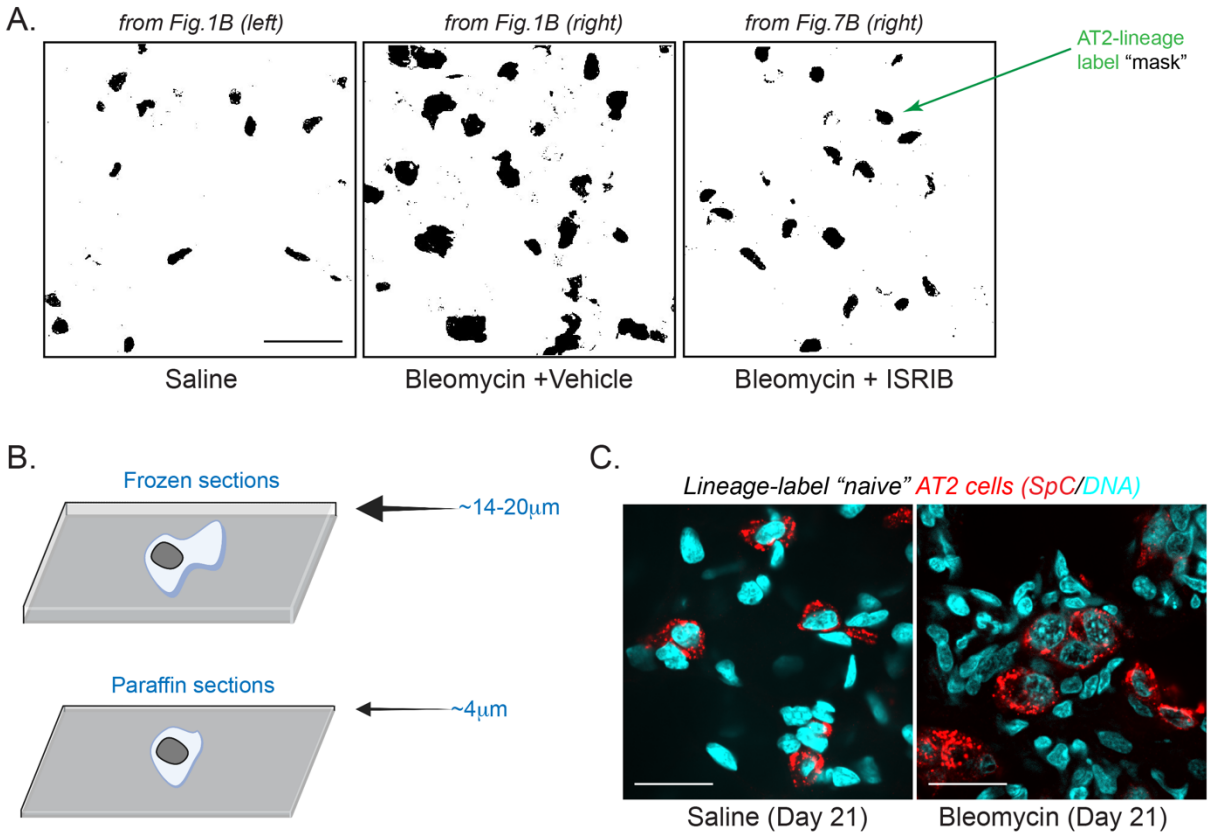

658

659 **Figure 2**: **Lung injury induces polyploidization of lineage-labeled and SpC+ AT2 cells**. (**A**)
660 Schematic of experimental design as in Fig.1. Representative confocal images of lung sections
661 from bleomycin-treated mice; two independent fields of view from low and high-magnification
662 insets (boxed region) are shown (a' and a"). Native GFP fluorescence from AT2-lineage label
663 and immunofluorescence staining of AT1 cells by podoplanin (Pdpn, magenta). DNA labeling by
664 Hoechst (gray). Scale bar = 50μm and 10 μm for inset. Asterisks show suspected binucleated
665 AT2 cells. Arrows show plan of optical z-section, revealing that nuclei appear to touch in these
666 cells. Magenta arrow in a' indicates podoplanin signal in binucleated cells. SpC+ binucleated
667 AT2 cells are shown in Fig. S2F. (**B**) Graph shows quantification of AT2 cell binucleation. Data
668 points are from two mice, 5 fields of view per condition. Mean +/- SD. $p < 0.0001$ by t-test.
669 Injury-induced binucleation was also interrogated by flow cytometry in Fig. S2A-E.
670
671

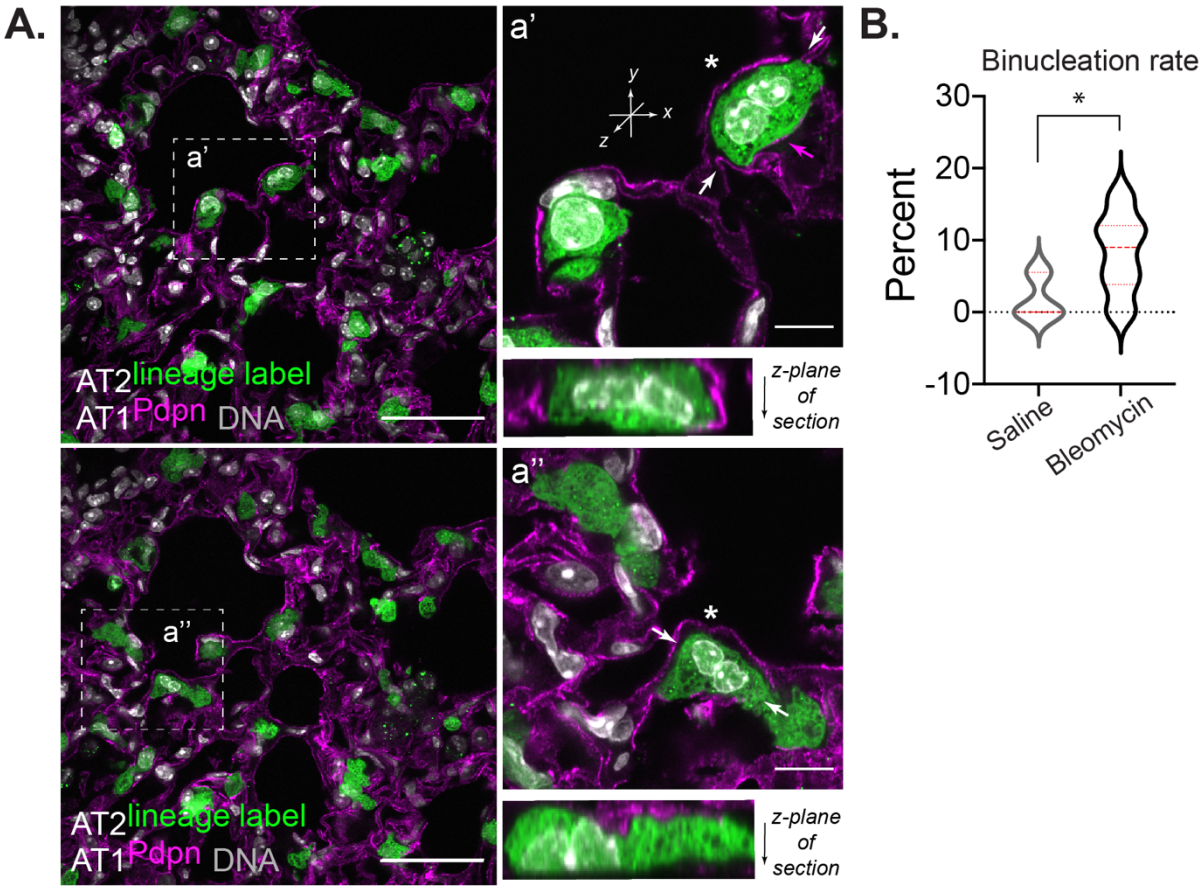

672
673

674 **Figure S2**: **Quantification of injury-induced AT2 hypertrophy and binucleation by flow**
675 **cytometry**. (**A**) Schematic of experimental design. (**B**) Young adult mice (3-5 months) were
676 administered saline alone or 0.025 units of bleomycin and lungs were harvested and digested
677 for flow cytometry on Day 12 with representative flow plots gated on CD45-/Epcam+ AT2 cells
678 with 2N (diploid, red) or 4N DNA content (cyan) (Methods). (**C**) Quantification of AT2 cell size
679 (median Forward Scatter Area). (**D**) Percent 2N versus 4N AT2 cells. N = 3 mice. p = 0.0008
680 and 0.0039 by ANOVA with Tukey's. (**E**) Validation of bleomycin-induced AT2 cell size increase
681 and binucleation by cytospin analysis. Cellular F-actin stained with phalloidin (green) to
682 distinguish *bona fide* binucleation, with absence of F-actin-rich cell-cell junction between nuclei.
683 (**F**) Binucleated AT2 cells can be SpC+. Confocal z-stack image of Vibratome-cut 200μm thick
684 lung section from a C57BL/6 mouse with clearing (SHIELD method) immunofluorescence
685 detection of SpC (red) and nuclei (Draq5; cyan). Double arrowhead implicates two binucleated
686 AT2 cells in the same field of view.
687
688

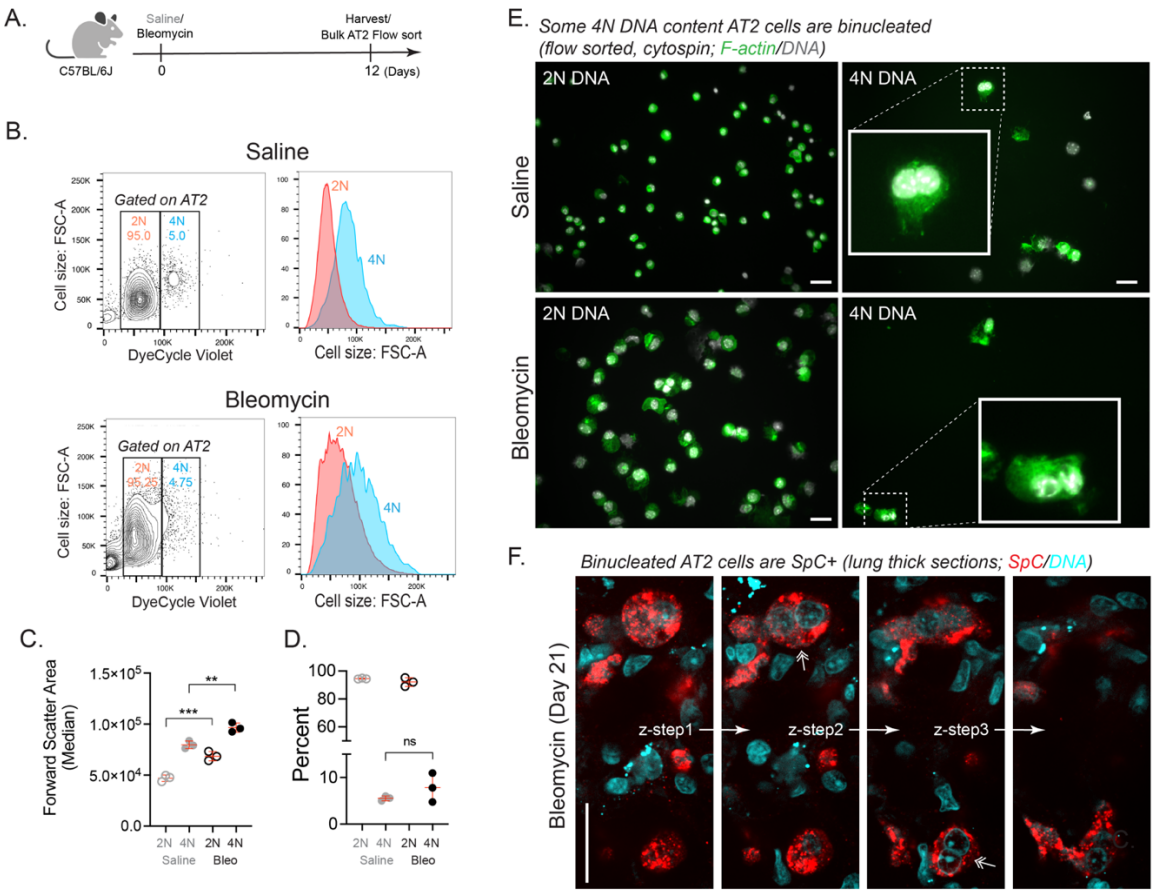

689

690 **Figure 3**: **AT2 cell binucleation is not universally associated with Krt8-high expression**
691 **phenotype.** (**A**) Schematic of experimental design as in Fig.1. Confocal image of lung section
692 from bleomycin-treated mice; same image as Figure 2A, now including Krt8
693 immunofluorescence channel (cyan). Asterisk denotes binucleated AT2 cell with normal levels
694 of Krt8 protein. Native GFP fluorescence from AT2-lineage label and immunofluorescence
695 staining of AT1 cells by podoplanin (Pdpn, magenta). DNA labeling by Hoechst (gray). (**B**)
696 Confocal image of binucleated Krt8-high cell (asterisk) lacking AT2 lineage-label. Scale bar =
697 50μm and 25 μm for inset. (**C**) Confocal image of lineage-labeled binucleated AT2 cell adjacent
698 to lineage negative mononuclear Krt8-high cell (z-stack not shown). Scale bar = 25μm.
699
700

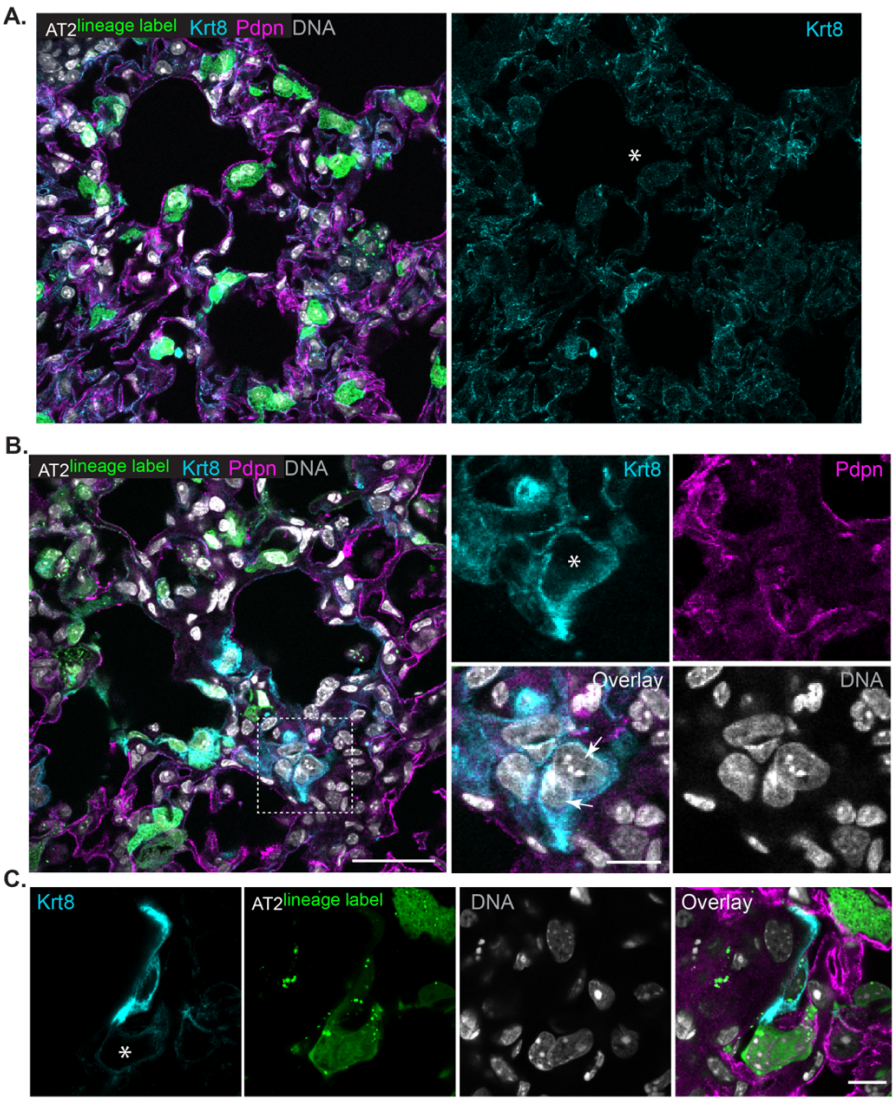

701
702

Figure S3: Identification of rare ≥4N AT2 cells via stochastic multi-color Confetti-labeling system. (**A**) Schematic adapted from (29) using *Sftpc*$^{\text{Cre-ER; R26R-Confetti}}$ strain (8). (**B**) Tamoxifen activation of *Sftpc*-targeted lineage-label at days 6-7 post-bleomycin injury and harvested Day 21. (**C**) Confocal image of thick-section cleared (SHIELD) lung, maximum z-projection of 3 slices showing rare GFP/RFP dual-positive cells, suggesting mononuclear polyploidy from partial nuclear exclusion of signal. The enlarged/flattened size of this cell (>25μm) is also compatible with 4N polyploidy. (**D**) Lower magnification view maximum z-projection (40 planes) shows that most lineage labeled cells are either GFP or RFP positive, with very few GFP/RFP-dual-positive cells (see inset showing gray cell, which reflects overlay of GFP/RFP). As this cell is ~10μm, it likely reflects a G2-phase AT2 cell with 4N DNA content. Asterisk validates bleomycin injury showing RFP lineage label along flattening AT1 cells.

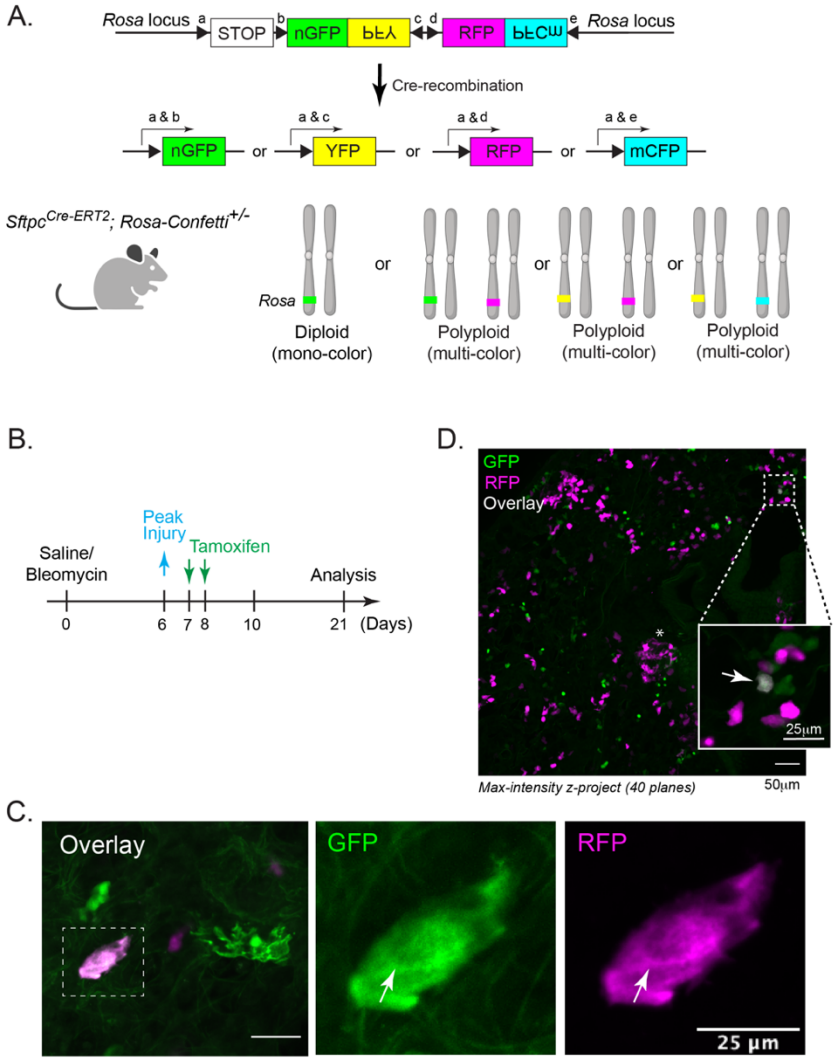

715 **Figure 4**: **Binucleation is a feature of AT2 cell cultures and organoids.** (**A**) Confocal images
716 of mouse AT2 cells grown 4 days on glass and rat AT2 cells grown 10 days on filters. Cells
717 were fixed and stained with Hoechst (DNA in cyan or gray), phalloidin (F-actin, green), Krt8
718 (green) or β-catenin (red) as indicated. Dotted lines (white) outline binucleated cells. (**B**)
719 Schematic for activation of AT2-lineage label before AT2 isolation. (**C**) Confocal image of
720 lineage-labeled AT2 cell (yellow) grown 3 days on glass. Arrow indicates binucleated, AT2-
721 derived cell. F-actin in cyan. (**D**) Schematic for activation of AT2-lineage label before AT2
722 isolation for organoid growth. (**E**) AT2 cell (green), F-actin (magenta) and DNA (gray) with
723 lineage-labeled binucleated cell (arrow). (**F**) Rate of AT2 binucleation in organoids. Scale bars =
724 50μm.
725

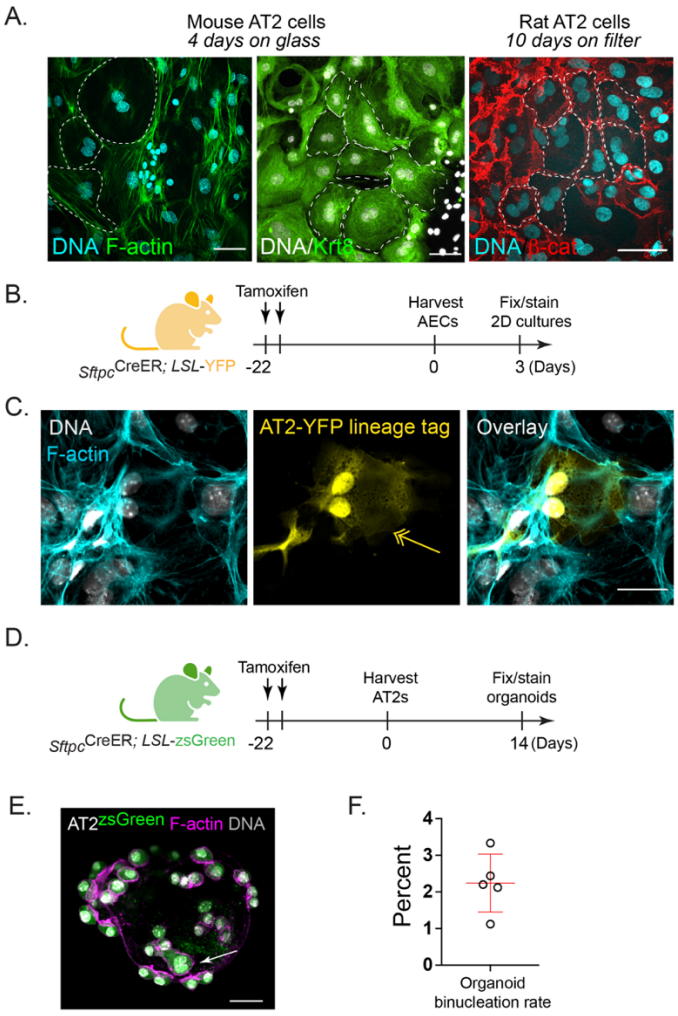

726

727 **Figure 5**: **AT2 cell binucleate via failed cytokinesis.** Murine AT2 cells were isolated and
728 phase-contrast live-imaged every 15-minutes (Methods). Time stamp and evident cell-cycle
729 phases are shown in cyan. Arrow indicated dividing cell.

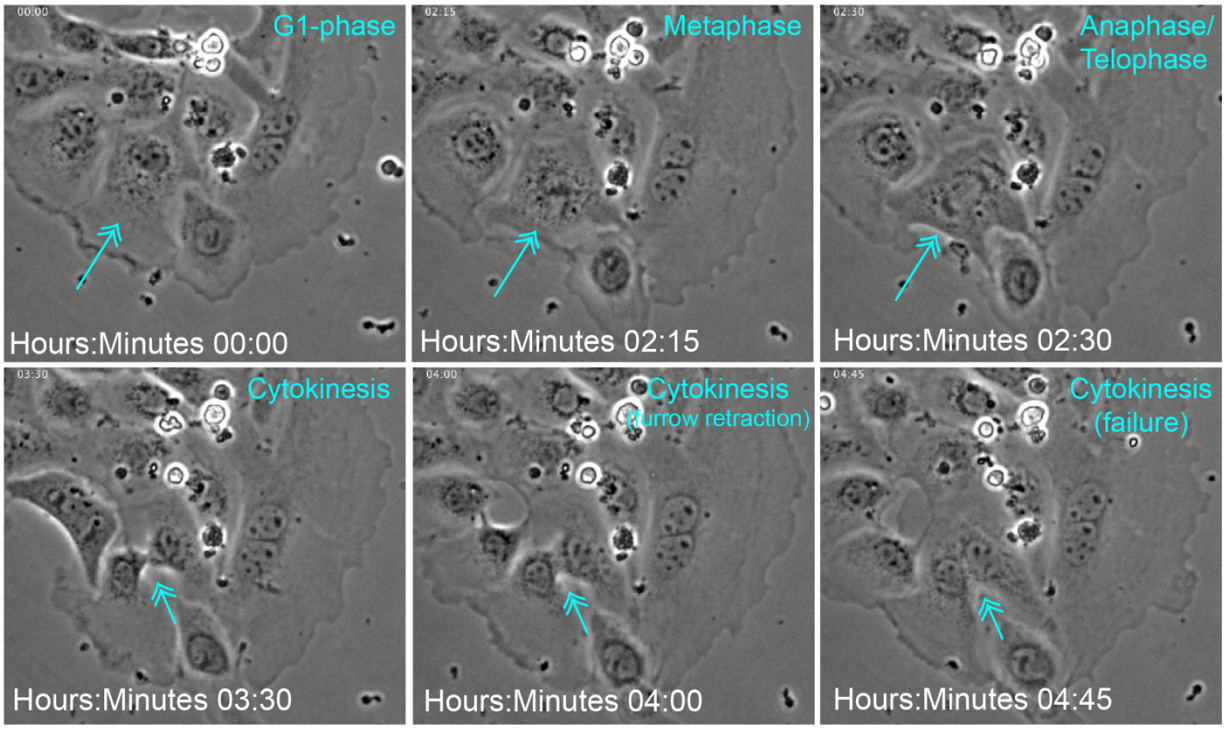

730

731 **Figure 6**: **ISRIB limits AT2 hypertrophy and polyploidy cell-autonomously**. (**A**) Schematic
732 for AT2 lineage-trace before bleomycin-injury with and without ISRIB therapy. (**B**) Confocal
733 images of fixed frozen lung sections with native zsGreen and immunofluorescence of AT1
734 marker, podoplanin. Scale 50μm. (**C**) Scatter plot of zsGreen object sizes by FIJI as described
735 in Figure S1. Graph identical to Fig.1C with ISRIB data added. Significance by ANOVA. (**D**)
736 Epifluorescence overlay images of mouse AT2 cell Day2-cultures incubated with Vehicle/ISRIB
737 (0.025μm) through Days 4-5. Arrows (magenta) show podoplanin+ binucleated cells that are
738 peripheral to large flat bi-/tri-nucleated cells with diminishing podoplanin and high levels of β-
739 catenin (white arrow). Scale 50μm. (**E**) Nuclear area (DNA) measurements by ImageJ as proxy
740 for cell size allowed for unbiased analysis. N = 6829 (Vehicle) and 7387 (ISRIB) nuclei
741 measured. Data averaged from 3 independent AT2 isolations for cells quantified at 48 and 72-
742 hours +/- ISRIB. p < 0.0001**** by Mann-Whitney test. (**F**) Histogram of data in **E**. (**G**)
743 Binucleation events quantified as from 44 (Vehicle) and 43 (ISRIB) fields of view. p = 0.035* by
744 Mann-Whitney test.

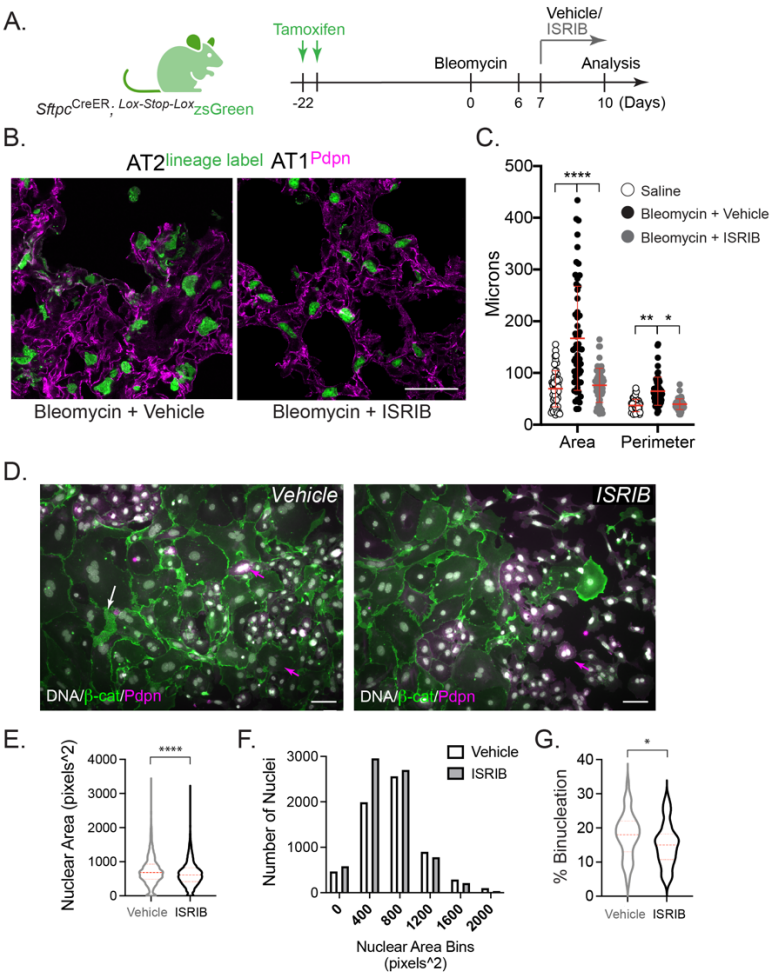

745
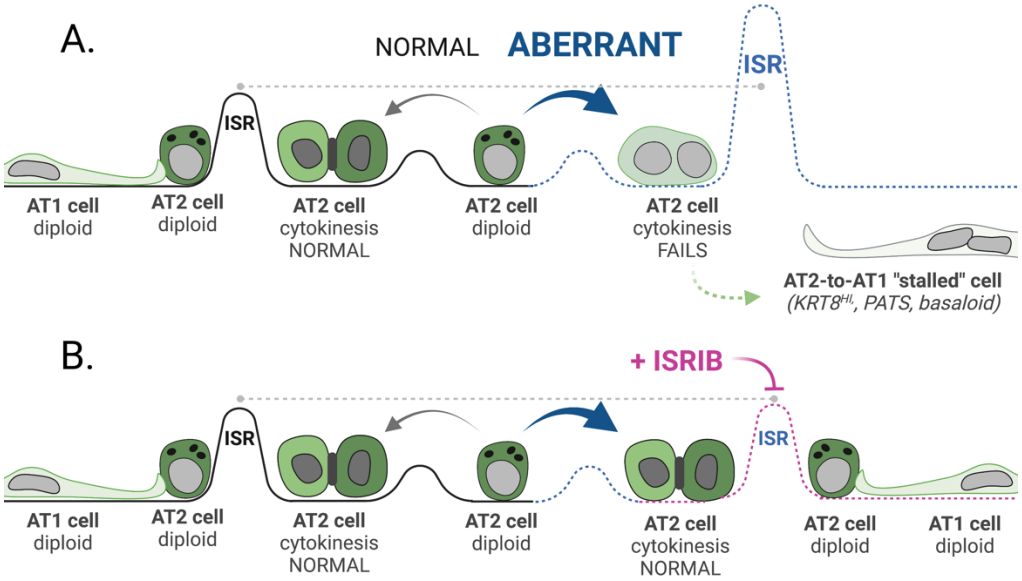
Figure 7: **Model for alveolar epithelial stress-induced polyploidization in lung injury and repair.** (**A**) AT2 "aberrant" repair (dotted blue line) due to persistent ISR, AT2 cytokinesis failure and stalled AT2-to-AT1 cells (right). (**B**) ISRIB therapy (dotted pink line) restores ISR to levels for normal AT2-to-AT1 differentiation (dotted gray line).